DSOSR: DEGRADATION-SEPARATED REAL-WORLD OMNIDIRECTIONAL IMAGE SUPER-RESOLUTION VIA PROJECTION FUSION REPRESENTATION

Anonymous authorsPaper under double-blind review

000

001

002

004

006

008 009 010

011

013

014

016

017

018

019

021

023

025

026

027

028

029

031

034

039

040 041

042

043

044

045

047

048

051

052

ABSTRACT

With the growing demand for immersive visual experience in virtual and augmented reality, high-resolution (HR) and high-quality (HQ) omnidirectional images (ODIs) are becoming increasingly essential. However, the limited capabilities of capturing device and transmission bandwidth constrain ODI resolution, hindering the rendering of fine 360° details. This challenge is further compounded by unknown real-world degradations and geometric distortions, which severely degrade ODI visual quality. Although real-world super-resolution (Real-SR) has been widely studied, existing degradation simulations fail to accurately characterize the complex imaging pipeline of ODIs. In practice, ODIs are usually collected by fisheye cameras and projected from the sphere to a plane through Equirectangular Projection (ERP), which introduces aliasing and domain-specific distortions. To bridge this gap, we propose a Degradation-Separated real-world Omnidirectional image Super-Resolution (DSOSR) framework that explicitly models the combined degradations from fisheye imaging and ERP projection. DSOSR is built upon two key insights: (1) projection degradations with strong priors significantly affect the distribution of random degradations, and (2) human attention in immersive scenarios typically focuses on local attractive viewpoints. Motivated by these observations, we develop a Perspective Projection Representation (PPR) to extract viewpoint features in parallel with the ERP branch, thereby isolating aliased degradations across domains. A Degradation-Specific Module (DSM) is then incorporated to separately modulate ERP-induced intrinsic geometric distortions and PPR-induced random real-world degradations. Furthermore, a Projection Fusion Attention Module (PFAM) is introduced to exploit inter-dependencies between ERP and PPR features, enabling more effective fusion of complementary representations. Extensive experiments demonstrate that the proposed DSOSR achieves state-of-the-art performance, delivering visually compelling and highfidelity omnidirectional Real-SR results for practical applications.

1 Introduction

Omnidirectional images (ODIs), also referred to as 360° or panoramic images, capture the full 360° field of view (FoV), thereby providing highly immersive and realistic visual experiences. With the rapid development of virtual and augmented reality applications, the demand for immersive ODIs has surged. To deliver a vast perspective, ODIs must be rendered at sufficiently high resolutions, such as 4K, 8K, or even 16K. Meanwhile, local regions that users typically focus on (ranging from $100^{\circ} \times 100^{\circ}$ to $120^{\circ} \times 120^{\circ}$ (Dasari et al., 2020)) should remain clear and detailed. However, most ODIs suffer from limited resolution due to the high cost of high-precision capturing devices and transmission bandwidth. Moreover, throughout the practical imaging pipeline—including acquisition, stitching, projection, transmission, processing, and viewing—ODIs are further degraded by blur, noise, down-sampling, compression artifacts, and projection distortions, all of which significantly reduce visual fidelity. Among these challenges, achieving high-resolution (HR) reconstruction remains the most fundamental requirement. Super-Resolution (SR) is a commonly adopted solution on the client side to enhance ODI quality. Nevertheless, most existing SR methods (Dong et al., 2014; Lim et al., 2017; Ledig et al., 2017; Zhang et al., 2018; Chen et al., 2023; Tian et al.,

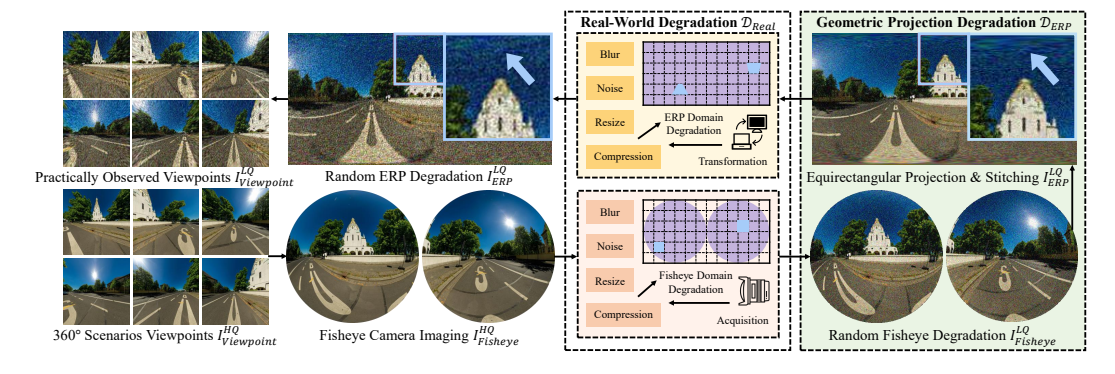


Figure 1: Real-world ODI degradations across the imaging pipeline. During the process of capturing fisheye ODIs and converting them into ERP representations, random degradations like blur, noise, resizing, and compression emerge. These effects are further compounded by projection-related distortions, including geometric stretching and deformation, which intensify artifacts and severely impair visual quality. It can be observed from the zoom-in regions that fisheye and ERP projections exhibit distinct degradation distributions.

2024) rely on the assumption of ideal Bicubic down-sampling, which deviates considerably from real-world degradations and thus limits their generalization ability. To this end, several real-world super-resolution (Real-SR) approaches (Cai et al., 2019; Wang et al., 2021a; Zhang et al., 2021; Wang et al., 2021b; Wei et al., 2021; Liang et al., 2022; Chan et al., 2022) either implicitly learn degradation priors from low-resolution (LR) images or explicitly synthesize LR-HR pairs to approximate real-world distributions. However, these methods overlook the broader range of degradations encountered in the ODI imaging chain, where mixed degradation distributions significantly challenge the restoration of photo-realistic high-quality ODIs.

ODIs are captured using fisheye cameras and stitched to cover the entire 360° space. To enable compatibility with conventional image transmission and processing pipelines, spherical ODIs are projected onto planar formats. This pixel-wise mapping inevitably leads to information loss and interpolation distortions. Despite the emergence of novel projection techniques, Equirectangular Projection (ERP) is still the most widely utilized due to its low computational complexity and broad applicability, as ERP images can be directly treated as generic 2D images with non-uniform content density. After projection, ERP ODIs are subject to compression, transmission, and enhancement before being back-projected onto the sphere for viewing localized perspective regions. As illustrated in Fig. 1, various types and levels of real-world degradations \mathcal{D}_{Real} arise throughout the ODI imaging pipeline, while ERP further introduces geometric distortions \mathcal{D}_{ERP} , leading to complex degradation distributions. Recent ODI-SR methods (Ozcinar et al., 2019; Deng et al., 2021; 2022; An & Zhang, 2023; Wang et al., 2024; Ji et al., 2024; Yang et al., 2025; Shen et al., 2025) mainly address ERP distortion by exploiting latitude-related geometric priors. Beyond these, OSRT (Yu et al., 2023) considers ODI formation and designs a fisheye-based down-sampling strategy, FATO (An et al., 2024) models the non-uniform ERP content distribution via fine-grained frequency representation, and OmniSSR (Li et al., 2024a) leverages planar generative priors within diffusion models for zero-shot ODI-SR. While these approaches partially alleviate projection and down-sampling degradations, they remain limited in covering the full spectrum of real-world scenarios, thus constraining both performance and generalization.

To overcome the challenges of real-world ODI-SR, we propose a combined fisheye-ERP degradation model to synthesize more realistic training samples that capture distortions across different degradation distributions. Considering the inherent complexity and diversity of ODI degradations, we design a dual-branch architecture that separately handles latitude-related projection distortions and blind pixel-level degradations. Specifically, a high-fidelity perspective projection representation branch is employed in parallel with the ERP branch to enhance viewpoint visual quality. In addition, degradation-specific encoding is applied to guide both branches in modulating distortions with and without location priors. Finally, a projection fusion mechanism is integrated to aggregate complementary information across reconstructed feature domains. The main contributions of this paper are summarized as follows:

- 1. We propose a mixed Fisheye-ERP degradation model that realistically simulates practical ODI distortions across the real-world application workflow—acquisition, stitching, projection, transmission, processing, and viewing. By explicitly separating degradations with different priors, our approach achieves more faithful restoration.
- 2. We introduce a Perspective Projection Representation (PPR) for continuous sampling that maps ERP ODIs into the perceptual viewing domain. The PPR effectively decouples geometric distortions and enables accurate modulation of real-world degradations observed in practical viewpoints.
- 3. We design a dual-branch network based on ERP and PPR representations, equipped with Degradation-Specific Modules (DSMs) to adaptively compensate for degradations in different distributions. Furthermore, a Projection Fusion Attention Module (PFAM) is developed to facilitate cross-branch interaction and enhance restoration performance.

2 RELATED WORK

108

110

111

112

113

114

115

116

117

118

119

120 121

122 123

124 125

126

127

128

129

130

131

132

133

134

135

136

137

138

139

140

141

142

143

144 145

146 147

148

149

150

151

152

153

154

155

156

157

158

159

160

161

2.1 REAL-WORLD IMAGE SUPER-RESOLUTION

With the rapid progress of deep learning, network-based image super-resolution (SR) models (Dong et al., 2014; Lim et al., 2017; Ledig et al., 2017; Zhang et al., 2018; Chen et al., 2023; Tian et al., 2024) have replaced traditional methods. However, these approaches always assume predefined degeneration types with fixed patterns, which fail to accurately reflect the complex and diverse degradation characteristics presented in real-world low-resolution (LR) images. In practice, LR images are acquired under diverse device conditions and environments, and are inevitably affected by blur, noise, resizing, and compression. To narrow the gap between synthetic and real-world degradations, a series of works have explored real-world super-resolution (Real-SR). RealSR (Cai et al., 2019) constructed a large kernel pool to cover diverse degradation types. BSRGAN (Zhang et al., 2021) and Real-ESRGAN (Wang et al., 2021b) explicitly built a mathematical degradation pipeline for more realistic synthesis. Son et al. (2021) simulated unknown down-sampling processes through adversarial training. DASR (Liang et al., 2022) adaptively estimated degradation information from LR inputs and employs it to modulate network parameters. LWay (Chen et al., 2024) bridged the synthetic-real gap by combining supervised pre-training with self-supervised learning. DKP (Yang et al., 2024) designed an unsupervised kernel estimation strategy based on a Markov chain Monte Carlo sampling. AdaSR (Fan et al., 2024) leveraged sample-adaptive priors learned through image self-similarity. More recently, diffusion-based models (Lin et al., 2024; Wu et al., 2024; Yu et al., 2024) have achieved remarkable improvements by introducing photorealistic generative priors. Nevertheless, such models inherit the substantial computational cost of diffusion backbones, which makes scaling to ultra-high-resolution ODIs particularly challenging.

2.2 Omnidirectional Image Super-Resolution

Several methods have been proposed to address the unique distortions in omnidirectional image super-resolution (ODI-SR). Ozcinar et al. (2019) first considered the latitude-related distortions of ERP and optimized the loss function accordingly. LAU-Net (Deng et al., 2021) revealed that ERP ODI pixels are unevenly distributed across latitudes and introduced a hierarchical processing strategy, which was further improved in LAU-Net+ (Deng et al., 2022) by adding a lightweight high-latitude enhancement module and a bidirectional loss. SphereSR (Yoon et al., 2022) designed an icosahedron-based feature extraction module to predict continuous coordinate transformations between spherical and arbitrary projection formats. An & Zhang (2023) proposed a perceptionoriented network that enhances viewpoints observed with high frequency. Subsequent works investigated more advanced strategies. OSRT (Yu et al., 2023) aligned features through continuous and adaptive offsets to mitigate ERP distortions, while GDGT-OSR (Yang et al., 2025) extended this idea with a distortion-modulated rectangle-window self-attention mechanism to better capture self-similar textures. FATO (An et al., 2024) explored the frequency-domain distribution of ODIs and introduced a high-frequency attention module to deal with content density imbalance. BPOSR (Wang et al., 2024) jointly utilized ERP and cubemap projections through a parallel attention mechanism, exploiting the complementary properties of different formats. ODA-SRN (Ji et al., 2024) proposed multi-segment parameterized convolutions to generate dynamic filters that compensate for

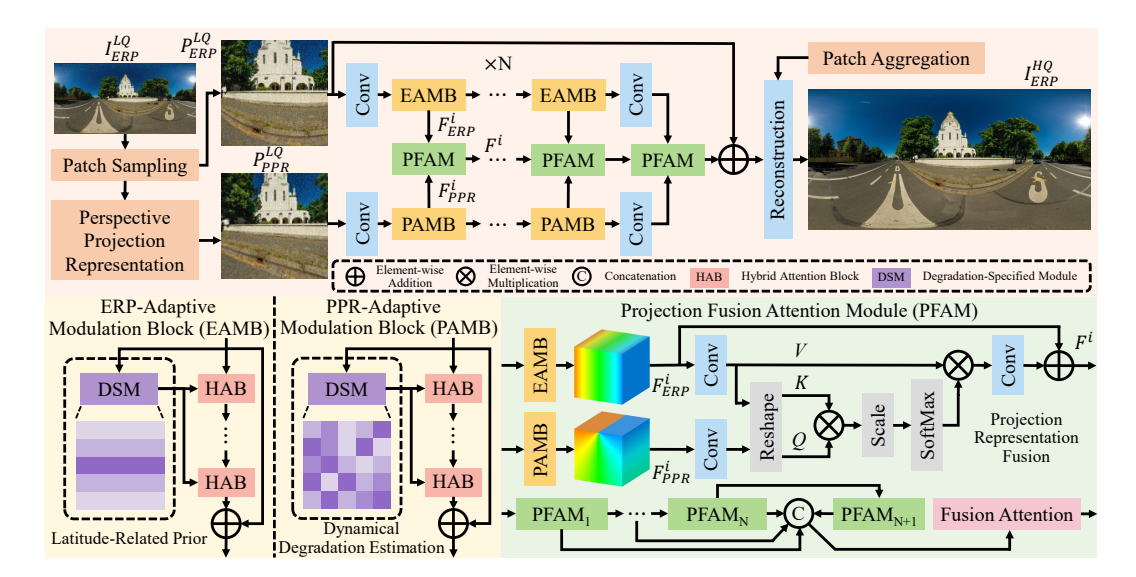


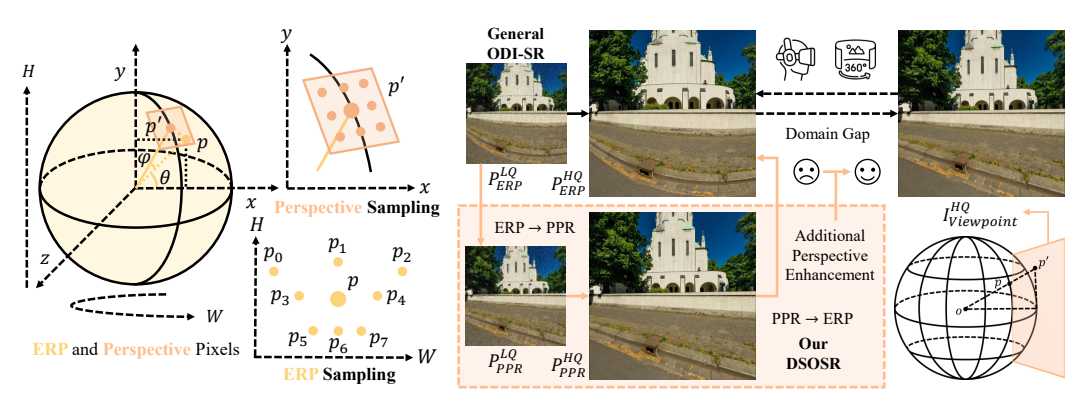
Figure 2: The overall framework of the proposed DSOSR. It consists of two parallel branches: an ERP branch and a PPR branch. Specifically, PPR patches are transformed from ERP patches in a nearly lossless manner, ensuring consistent content across both representations. The PPR branch extracts features under the distribution of human visual perspective, thereby enhancing perceptual realism. To handle different degradation sources, DSMs are embedded in both branches: the ERP branch adaptively compensates for geometric projection distortions, while the PPR branch focuses on random real-world degradations in local viewpoints. Finally, the PFAMs aggregate and re-weight the restored features from the two branches, enabling supplementary information exchange and generating high-quality reconstructions.

geometric distortions during feature extraction. FAOR (Shen et al., 2025) incorporated spherical geometric priors to adapt implicit image functions from the planar domain to ERP images. OmniSSR (Li et al., 2024a) introduced octadecaplex tangent interaction and gradient decomposition to achieve zero-shot ODI-SR. Despite these advances, most existing methods primarily focus on geometric ERP distortions under the assumption of fixed bicubic down-sampling. They ignore the degradation characteristics of real-world ODIs as well as the distribution patterns of human visual perception across local viewpoints. These limitations hinder the practical applicability of ODI-SR methods and restrict their ability to deliver truly immersive experiences.

3 METHOD

3.1 OVERALL FRAMEWORK

The pipeline of DSOSR is demonstrated in Fig. 2. Given a low-quality (LQ) ERP image I_{ERP}^{LR} with both geometric and real-world degradations, the objective is to learn an adaptive model \mathcal{M} that can modulate aliased degradations \mathcal{D}_{ERP} and \mathcal{D}_{Real} while restoring high-resolution details. Formally, $I_{ERP}^{LQ} \in \mathbb{R}^{H \times W \times C}$ is partitioned into patches $P_{ERP}^{LQ} \in \mathbb{R}^{h \times w \times C}$ with positional information. To decouple degradation types, the Perspective Projection Representation (PPR) transforms ERP patches into perspective patches $P_{PPR}^{LQ} \in \mathbb{R}^{h \times w \times C}$, thereby isolating \mathcal{D}_{ERP} and focusing on alleviating \mathcal{D}_{Real} . Both ERP and PPR patches are first encoded through 3×3 convolutions to generate shallow features F_{ERP}^0 and F_{PPR}^0 . These are then fed into two parallel branches: the ERP branch with N ERP-Adaptive Modulation Blocks (EAMBs), and the PPR branch with N PPR-Adaptive Modulation Blocks (PAMBs). Each block is built upon multiple Hybrid Attention Blocks (HABs, (Chen et al., 2023)) and augmented with a Degradation-Specific Module (DSM). DSMs in EAMBs estimate projection-induced degradation \mathcal{D}_{ERP} and compensate for latitude-related distortions, while DSMs in PAMBs emphasize real-world degradation \mathcal{D}_{Real} for improving viewpoint-consistent features. Furthermore, Projection Fusion Attention Modules (PFAMs) are inserted at each stage to aggregate features F_{ERP}^i and F_{PPR}^i across the two branches. The outputs from PFAM₁ to



(a) ERP and PPR distributions.

(b) The PPR branch in DSOSR.

Figure 3: (a) Illustration of pixel distributions in Equirectangular Projection (ERP) and Perspective Projection Representation (PPR). The higher latitudes correspond to more dispersed pixels. (b) PPR converts ERP patches into perspective patches, aligning viewing distributions and effectively decoupling projection degradations.

 $PFAM_{N+1}$ are progressively fused through an additional attention module, yielding the final high-quality reconstruction.

3.2 Perspective Projection Representation (PPR)

ERP achieves the space-to-plane transformation but brings distortions in polar regions. When such geometric degradations are aliased with real-world degradations accumulated at different stages of the ODI imaging pipeline (Fig. 1), recovering clean content becomes highly challenging. To address this issue, we introduce a perspective branch that processes features without projection interference and is more consistent with human viewing distributions. However, existing transformation methods rely on interpolation, which results in blurred representations. Therefore, we creatively propose a Perspective Projection Representation (PPR) that enables nearly lossless mapping.

As shown in Fig. 3(a), the projection between ERP and PPR is formulated along the cutting plane direction. Specifically, an ERP coordinate grid is first mapped onto the spherical surface, followed by a rotation matrix applied at the sphere center o to simulate camera rotations. The tangent plane at the rotated viewpoint (orange region) is then back-projected to the ERP pixel coordinates, yielding the transformation ERP \rightarrow Sphere \rightarrow PPR. Nevertheless, current resampling strategies (e.g., Bicubic or Bilinear interpolation) depend on intermediate spherical warping, which inevitably introduces information loss. Inspired by findings that orientation and curvature based spatially varying priors contribute to enhance representational capacity (Lee et al., 2022), we develop an accurate perspective representation to explicitly decouple projection degradations from real-world distortions. For a target PPR position p'(u',v') corresponding to an ERP position p(u,v), we assume a continuous mapping function p'=f(p). The local grid $\delta p'$ is estimated by considering p and its neighbor set p in different directions. p is a set p is a set p in different directions. p is a set p in different directions can be calculated as:

$$\delta p_i' = f(p) - f(p_i) \approx f(p_i) + J_f(p_i)(p - p_i) - f(p_i) = J_f(p_i)(p - p_i) = J_f(p_i)\delta p,$$
 (1)

where $J_f(p_i) \in \mathbb{R}^{2 \times 2}$ denotes the Jacobian matrix of f at p_i , and $\delta p = p - p_i$ is the local grid in ERP space. Since ERP-to-PPR mapping varies across spherical latitudes, higher-order priors are necessary to capture arbitrary warping. Following Lee et al. (2022); Li et al. (2024b), we further incorporate the second-order Hessian matrix $H_f(\mathcal{P}) \in \mathbb{R}^{2 \times 2 \times 2}$ with the first-order Jacobian matrix to provide the orientation and curvature priors. Based on such geometric descriptions, we approximately simulate $\delta p' = J_f(\mathcal{P})\delta p$, and $\delta(\nabla p') = H_f(\mathcal{P})\delta(\nabla p)$:

$$J_f(\mathcal{P}) = \begin{bmatrix} p_4' - p_3' \\ p_1' - p_6' \end{bmatrix}, \ H_f(\mathcal{P}) = \begin{bmatrix} p_3' + p_4' - 2p' & p_2' + p_5' - p_0' - p_7' \\ p_2' + p_5' - p_0' - p_7' & p_1' + p_6' - 2p' \end{bmatrix}.$$
(2)

Figure 4: (a) DSM generates adaptive guidance tailored to different projection distributions. (b) The attention-based fusion of the Projection Fusion Attention Module (PFAM).

Unlike previous works that adopt Jacobian and Hessian matrices merely for pixel warping, we provide a quantitative description of the ERP-PPR conversion in terms of $\delta p'$ and $\delta(\nabla p')$ without resorting to intermediate spherical coordinates. More precisely, we concatenate the six matrix elements as spatial priors $s(\mathcal{P})$, which and allow us to accurately represent the ERP-PPR mapping without extraditional spherical resampling. Inspired by the implicit neural representation works (Chen et al., 2021; Son & Lee, 2021; Lee et al., 2022), we predict PPR pixels p_i from the latent space of ERP pixels p_i , guided by $s(\mathcal{P})$. To achieve this, we design a learnable coordinate transformation estimator $E = \{E_a, E_f, E_p\}$ that captures local textures in the 2D Fourier domain Lee et al. (2022). The pixel estimation form ERP to PPR can be expressed as follows:

$$E(\mathcal{E}(p), \delta p, s(\mathcal{P})) = E_a(\mathcal{E}(p)) \otimes \begin{bmatrix} \cos\{\pi(\langle E_f(\mathcal{E}(p)), \delta p > + E_p(s(\mathcal{P})))\} \\ \sin\{\pi(\langle E_f(\mathcal{E}(p)), \delta p > + E_p(s(\mathcal{P})))\} \end{bmatrix}, \tag{3}$$

where $\mathcal{E}(\cdot)$ indicates a feature encoder, E_a , E_f , and E_p estimate amplitude, frequency, and phase, respectively. Here, $<\cdot,\cdot>$ means the inner product. Based on this estimator, the PPR pixel distribution is predicted as:

$$P_{PPR}^{LQ} = \operatorname{Up}(P_{ERP}^{LQ}) + \sum_{i \in \mathcal{P}} \omega_i \mathcal{D}(E(\mathcal{E}(p), \delta p, s(p_i))), \tag{4}$$

where $\mathrm{Up}(\cdot)$ is Bilinear up-sampling to facilitate stable model convergence and ω_i is a local ensemble coefficient. Instead of directly utilizing interpolation-based mappings (e.g., OpenCV Remap), our PPR formulation mitigates information loss from direct ERP-to-PPR transformation. As depicted in Fig. 3(b), the resulting PPR images are processed as an additional branch, effectively isolating geometric ERP degradations, emphasizing real-world distortions, and better aligning with practical human viewing distributions.

3.3 DEGRADATION-SPECIFIC MODULE (DSM)

As illustrated in Fig. 2, we design two complementary modules, the ERP-Adaptive Modulation Block (EAMB) and the PPR-Adaptive Modulation Block (PAMB), to address multi-degradation in ODIs. The EAMB focuses on features in the ERP domain and alleviates latitude-related projection distortions, while the PAMB concentrates on perspective-domain features to handle random real-world degradations. To further exploit domain-specific priors, we incorporate Degradation-Specific Modules (DSMs) into both branches, enabling effective degradation guidance across different projection distributions in real-world ODIs.

Fig. 4(a) shows the architecture of the proposed DSM. In the ith stage, the inputs to EAMB and PAMB are denoted as $F^i_{ERP} \in \mathbb{R}^{h \times w \times c_e}$ and $F^i_{PPR} \in \mathbb{R}^{h \times w \times c_p}$, respectively. Since the feature distributions vary with different projections in the $h \times w$ direction, we first capture the projection-specific degradation priors by embedding the integrated projection degradation via 1×1 CNNs. The detailed derivation of the latitude-related quantization map can be found in Appendix A.2. The embedded conditional map of size $h \times w \times 1$ is fused with the degraded feature F^i_{ERP} to obtain a geometrically calibrated representation $F^{i'}_{ERP}$. As we aim to achieve the distribution-depended estimation adaptively, we design a lightweight encoder to generate degradation descriptor vectors $D^i_{ERP} \in \mathbb{R}^{h_d \times w_d \times c_p d}$ and $D^i_{PPR} \in \mathbb{R}^{h_d \times w_d \times c_p d}$. Specifically, the features are first processed

by 3×3 CNNs with LeakyReLU activation, and then projected into descriptor vectors through Adaptive Average Pooling (AAP). These vectors are mapped back into the shape of $h_d \times w_d \times c_{ed}$ and $h_d \times w_d \times c_{pd}$ as masks, which are subsequently up-sampled and refined by CNNs to realize feature-level modulation. The generation of degradation-specific features in ERP and PPR branches is summarized as:

$$DSF_{ERP}^{i}/DSF_{FFR}^{i} = \text{Up}\left(\text{Conv}\left(\sum_{k=1}^{K} \text{AAP}(\text{Conv}(F_{ERP}^{i'}/F_{PPR}^{i}))_{k}P_{k}\right)\right), \tag{5}$$

where k represents the length of the descriptor vector. Finally, we concatenate the input features with the degradation-aware features and feed them into the Transformer block HAB (Chen et al., 2023), formulated as:

$$F_{ERP}^{i}/F_{FFR}^{i} = \operatorname{Conv}(\operatorname{HAB}(\operatorname{Cat}(F_{ERP}^{i}/F_{FFR}^{i}, DSF_{ERP}^{i}/DSF_{FFR}^{i}))). \tag{6}$$

3.4 Projection Fusion Attention Module (PFAM)

The aggregation and fusion of enhanced features across different distributions and stages have a significant impact on the final SR performance. As demonstrated in Fig. 2, the outputs of EAMBs and PAMBs originate from distinct projection domains and hierarchical depths, which poses challenges for effective integration. To address this, we propose a Projection Fusion Attention Module (PFAM) to achieve adaptive and robust feature fusion. The overall framework of PFAM is depicted in Fig. 2. We employ a self-attention mechanism to dynamically emphasize informative features while suppressing redundant or repeated ones. Specifically, we take F_{ERP}^i as the value matrix V and construct the key matrix metric as $K = V^{\top}$, and the query matrix Q is derived from F_{PPR}^{i} . By performing projection-guided attention, PFAMi produces the fused output F^i that effectively integrates F^i_{ERP} and F_{PPR}^{i} . The fused feature set is defined as \mathcal{F} of $\{F^{i}, i=0,1,...,N,N+1\}$, which aggregates information across multiple depths. To further compress and refine \mathcal{F} , we introduce a 3D attention module that jointly processes along the depth dimension. As shown in Fig. 4(b), the features in \mathcal{F} are concatenated and passed through the fusion attention block, enabling effective aggregation of multi-level and multi-distribution representations. In a word, PFAM serves as the bridge between the ERP and PPR branches, enabling the network to leverage complementary representations from different projection domains. By introducing attention-based fusion, PFAM not only reduces the risk of feature misalignment but also adaptively balances the contributions of geometric and realworld oriented representations. Together with DSM-guided modulation in EAMBs and PAMBs, PFAM ensures that DSOSR can fully exploit both projection-separated and depth-aware features, ultimately leading to more robust and accurate ODI super-resolution.

4 EXPERIMENTS

4.1 IMPLEMENTATION DETAILS

The proposed DSOSR presents a projection fusion representation based solution for real-world ODI-SR. To simulate the ODI degradations in practical scenarios, we utilize ODI datasets Flickr360(Cao et al., 2023) (training and testing), ODI-SR (Deng et al., 2021) (testing), and SUN360 (Xiao et al., 2012) (testing), where the resolution of HR ERP ODIs is 1024×2048 . Next, we generate random degradations (Fisheye and ERP distributions, indicated in Fig. 1) in the pre-partitioned datasets following the settings of Real-ESRGAN (Wang et al., 2021b). The number N of EAMBs and PAMBs is 4 with a depth of 6, the channels c_e and c_p are set to 60 and 30, respectively. In the DSMs, we set k=5, $c_{ed}=128$, and $c_{pd}=64$. We integrate one PFAM between every EAMB and PAMB to fuse features, and an additional PFAM after the final blocks. During training, HR ODIs are cropped to 256×256 patches and augmented with flip. We adopt a batch size of 8 and optimize DSOSR with the Adam optimizer ($lr=2\times 10^{-4}$, $\beta_1=0.9$, and $\beta_2=0.99$) for 200K iterations through the L1 loss function. The training is conducted on A6000 GPUs in PyTorch.

4.2 Comparison Results

To validate the effectiveness of the proposed real-world DSOSR network, we compare it with existing ODI-SR, Real-SR, and image restoration methods, including 360-SS (Ozcinar et al., 2019),

Dataset	Flickr3	660 Dataset	ODI-SR Dataset		
Method	PSNR (dB)↑ / SSIM↑	WS-PSNR (dB)↑/ WS-SSIM↑	PSNR (dB)↑/ SSIM↑	WS-PSNR (dB)↑/ WS-SSIM↑	
360-SS	24.20 / 0.6198	23.65 / 0.5963	23.30 / 0.6031	22.59 / 0.5712	
Real-ESRGAN	24.30 / 0.6171	23.77 / 0.5944	23.24 / 0.6001	22.50 / 0.5665	
SwinIR	25.16 / 0.6827	24.66 / 0.6628	23.97 / 0.6537	23.27 / 0.6242	
HAT	25.19 / 0.6838	24.68 / 0.6641	23.97 / 0.6541	23.27 / 0.6245	
PromptIR	25.20 / 0.6852	24.70 / 0.6648	24.00 / 0.6555	23.30 / 0.6256	
OSŔT	25.41 / 0.6886	24.92 / 0.6680	24.22 / 0.6569	23.54 / 0.6277	
BPOSR	25.34 / 0.6864	24.83 / 0.6651	24.14 / 0.6541	23.44 / 0.6244	
AdaIR	25.49 / 0.6912	24.98 / 0.6706	24.26 / 0.6591	23.57 / 0.6302	
DSOSR(Ours)	$\overline{25.64} / \overline{0.6934}$	$\overline{25.13}$ / $\overline{0.6726}$	24.37 / 0.6626	$\overline{23.67} / \overline{0.6334}$	

Table 1: Quantitative ×4 real-world ODI-SR comparison on Flickr360 and ODI-SR datasets. **Bold** and underlined values indicate the best and second-best results.



Figure 5: Qualitative ×4 real-world ODI-SR comparison on ERP ODIs.

OSRT (Yu et al., 2023), BPOSR (Wang et al., 2024), Real-ESRGAN (Wang et al., 2021b), SwinIR (Liang et al., 2021), HAT (Chen et al., 2023), PromptIR (Potlapalli et al., 2023), AdaIR (Cui et al., 2025). PSNR, SSIM, and ERP ODI-oriented WS-PSNR (Sun et al., 2017), WS-SSIM (Zhou et al., 2018) are calculated on the luma (Y) channel to conduct numerical comparison. Notably, the parts of mentioned approaches are not designed for the real-world ODI-SR task in their initial version. Therefore, we fairly retrain them in a unified training paradigm on the simulated real-world ODI-SR dataset. The training parameters are kept the same, and the only difference is the network architecture.

4.2.1 QUANTITATIVE AND QUALITATIVE COMPARISON

As displayed in Tab. 1, our DSOSR achieves the best quantitative metrics on all benchmarks, demonstrating its superior capacity. Notably, DSOSR overcomes the second-best approach AdaIR with 0.15 dB WS-PSNR on the Flickr360 dataset. More quantitative and computational efficiency comparison results are mentioned in Sec. A.3.

Fig. 5 presents visual results from representative ODI-SR and image restoration methods. Upon inspection of zoomed-in regions, only DSOSR effectively removes the artifacts aliased in LQ inputs. The grids and stripes of buildings in DSOSR are restored with better fidelity in the color distribution. In the second scene, no noticeable noise is generated around the picture in the DSOSR reconstruction. These observations corroborate that DSOSR reconstructs finer structural details and surpasses current methods.

4.3 ABLATION STUDIES

In this section, we perform ablation studies to validate the effectiveness of developed components individually. All ablation experimental settings follow the configuration of the full-scale DSOSR training on the $\times 4$ real-world ODI-SR task.

Table 2: Ablation studies for the parallel branch design and corresponding Perspective Projection Representation (PPR) on the real-world Flickr360 dataset.

Method	Single-branch	Dual-branch	ERP	Pers	PPR	PSNR / SSIM	WS-PSNR / WS-SSIM
Baseline	√		$\overline{}$			25.20 / 0.6858	24.63 / 0.6644
Perspective (Pers)	✓			\checkmark		25.09 / 0.6820	24.51 / 0.6602
Dual-Baseline		\checkmark	\checkmark			25.35 / 0.6865	24.77 / 0.6650
Baseline + Pers		\checkmark	\checkmark	\checkmark		25.47 / 0.6882	24.90 / 0.6669
Baseline + PPR		\checkmark	\checkmark		\checkmark	25.50 / 0.6892	24.94 / 0.6682

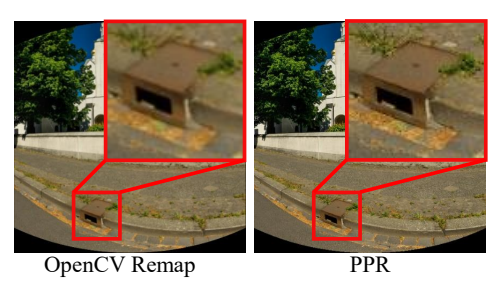


Figure 6: ERP-to-Perspective-to-ERP Results.

Table 3: Ablation studies for the Degradation-Specific Module (DSM) and Projection Fusion Attention Module (PFAM) on the real-world Flickr360 dataset.

Method	PSNR / SSIM	WS-PSNR / WS-SSIM
Baseline + PPR		
$+ DSM_{ERP}$	25.56 / 0.6906	25.02 / 0.6702
$+ DSM_{PPR}$	25.58 / 0.6909	25.03 / 0.6703
+ DSM _{ERP&PPR}	25.58 / 0.6910	25.06 / 0.6712
+ PFAM	25.60 / 0.6923	25.10 / 0.6719

Effects of different dual-branch architectures and projection representations. Tab. 2 demonstrates the performance benefits of several branch and representation architectures. It can be found that directly projecting ERP images into the perspective domain and processing features do not lead to performance enhancement. Directly replicating the network structure (halved dimension) to serve as an extra branch achieves 0.14 dB WS-PSNR improvements. Compared with the feature width expansion in the same distribution, the proposed parallel perspective branch provides complementary representations and brings 0.27 dB gains in the term of WS-PSNR. The further accurate PPR boosts the result to 24.94 dB WS-PSNR. These results corroborate the effectiveness of the dual-branch design in ERP and PPR representations. Moreover, we visualize the ERP-to-Perspective-to-ERP mapping processed by OpenCV Remap and PPR in Fig. 6. Compared to interpolation-based methods, when PPR ODIs are projected back to the ERP format, it is nearly lossless without blurring.

Impact of individual architecture modules. We conduct this ablation to further examine the proposed Degradation-Specific Module (DSM) and Projection Fusion Attention Module (PFAM) on the PPR-based dual-branch framework. We incrementally include individual components, and results are shown in Tab. 3. The joint introduction of DSM_{ERP} and DSM_{PPR} leads to a 0.1 dB WS-PSNR improvement. Meanwhile, the baseline method with PPR and PFAM reaches 25.10 dB WS-PSNR. The degradation guidance across different projection distributions and the following attention-based fusion facilitates the ability of DSOSR to handle real-world ODIs.

5 CONCLUSION

In this paper, we proposed a Degradation-Separated real-world Omnidirectional image Super-Resolution (DSOSR) network in practical scenarios. First, we modeled a realistic two-stage Fisheye-ERP degradation based on the ODI imaging pipeline. Motivated by the findings: (1) that geometric projection degradation aliases with the random distortions, and (2) users prefer limited viewpoints across the whole 360° space, we subsequently developed a Perspective Projection Representation (PPR) based dual-branch architecture to explicitly separate degradations in different distributions and match the human perception law. Moreover, we integrated Degradation-Specific Modules (DSMs) in both branches to adaptively extract degradation priors. The enhanced features are further aggregated through Projection Fusion Attention Modules (PFAMs) in each stage for facilitating information interaction. Extensive experimental results on different datasets demonstrated that DSOSR achieves the best real-world ODI-SR performance and is application-friendly with faster speed and practical viewpoint enhancement.

ETHICS STATEMENT

This work solely relies on publicly available and widely used benchmark datasets, and no private or personally identifiable information is involved. The experiments are conducted for the purpose of algorithmic comparison and performance evaluation, without any human or animal subjects. The research does not generate harmful, offensive, or unsafe content, and the proposed methods are designed for general computer vision applications without direct high-risk societal implications.

REPRODUCIBILITY STATEMENT

All datasets used in this study are publicly available super-resolution benchmark datasets. Upon publication, we will release the complete code and data-processing scripts, including training configurations, hyperparameters, and random seeds. The experiments can be reproduced on common GPUs without requiring special resources or non-public data.

REFERENCES

- Hongyu An and Xinfeng Zhang. Perception-oriented omnidirectional image super-resolution based on transformer network. In 2023 IEEE International Conference on Image Processing (ICIP), pp. 3583–3587. IEEE, 2023.
- Hongyu An, Xinfeng Zhang, Shijie Zhao, and Li Zhang. FATO: Frequency Attention Transformer for Omnidirectional Image Super-Resolution. In *Proceedings of the 6th ACM International Conference on Multimedia in Asia*, pp. 1–7, 2024.
- Jianrui Cai, Hui Zeng, Hongwei Yong, Zisheng Cao, and Lei Zhang. Toward real-world single image super-resolution: A new benchmark and a new model. In *Proceedings of the IEEE/CVF international conference on computer vision*, pp. 3086–3095, 2019.
- Mingdeng Cao, Chong Mou, Fanghua Yu, Xintao Wang, Yinqiang Zheng, Jian Zhang, Chao Dong, Gen Li, Ying Shan, Radu Timofte, et al. NTIRE 2023 challenge on 360° omnidirectional image and video super-resolution: Datasets, methods and results. In *Proceedings of the IEEE/CVF conference on computer vision and pattern recognition*, pp. 1731–1745, 2023.
- Kelvin CK Chan, Shangchen Zhou, Xiangyu Xu, and Chen Change Loy. Investigating tradeoffs in real-world video super-resolution. In *Proceedings of the IEEE/CVF Conference on Computer Vision and Pattern Recognition*, pp. 5962–5971, 2022.
- Haoyu Chen, Wenbo Li, Jinjin Gu, Jingjing Ren, Haoze Sun, Xueyi Zou, Zhensong Zhang, Youliang Yan, and Lei Zhu. Low-Res Leads the Way: Improving generalization for super-resolution by self-supervised learning. In *Proceedings of the IEEE/CVF Conference on Computer Vision and Pattern Recognition*, pp. 25857–25867, 2024.
- Xiangyu Chen, Xintao Wang, Jiantao Zhou, Yu Qiao, and Chao Dong. Activating more pixels in image super-resolution transformer. In *Proceedings of the IEEE/CVF conference on computer vision and pattern recognition*, pp. 22367–22377, 2023.
- Yinbo Chen, Sifei Liu, and Xiaolong Wang. Learning continuous image representation with local implicit image function. In *Proceedings of the IEEE/CVF conference on computer vision and pattern recognition*, pp. 8628–8638, 2021.
- Yuning Cui, Syed Waqas Zamir, Salman Khan, Alois Knoll, Mubarak Shah, and Fahad Shahbaz Khan. AdaIR: Adaptive all-in-one image restoration via frequency mining and modulation. In 13th International Conference on Learning Representations, ICLR 2025, pp. 57335–57356. International Conference on Learning Representations, ICLR, 2025.
- Mallesham Dasari, Arani Bhattacharya, Santiago Vargas, Pranjal Sahu, Aruna Balasubramanian, and Samir R Das. Streaming 360-degree videos using super-resolution. In *IEEE INFOCOM* 2020-IEEE Conference on Computer Communications, pp. 1977–1986. IEEE, 2020.
- Xin Deng, Hao Wang, Mai Xu, Yichen Guo, Yuhang Song, and Li Yang. LAU-Net: Latitude adaptive upscaling network for omnidirectional image super-resolution. In *Proceedings of the IEEE/CVF Conference on Computer Vision and Pattern Recognition*, pp. 9189–9198, 2021.
- Xin Deng, Hao Wang, Mai Xu, Li Li, and Zulin Wang. Omnidirectional image super-resolution via latitude adaptive network. *IEEE Transactions on Multimedia*, 25:4108–4120, 2022.
- Chao Dong, Chen Change Loy, Kaiming He, and Xiaoou Tang. Learning a deep convolutional network for image super-resolution. In Computer Vision–ECCV 2014: 13th European Conference, Zurich, Switzerland, September 6-12, 2014, Proceedings, Part IV 13, pp. 184–199. Springer, 2014.
- Zejia Fan, Wenhan Yang, Zongming Guo, and Jiaying Liu. Towards real-world super resolution with adaptive self-similarity mining. *IEEE Transactions on Image Processing*, 2024.
- Xiang Ji, Changqiao Xu, Lujie Zhong, Shujie Yang, Han Xiao, and Gabriel-Miro Muntean. Dual enhancement in odi super-resolution: adapting convolution and upsampling to projection distortion. In *Proceedings of the Thirty-Third International Joint Conference on Artificial Intelligence*, pp. 902–910, 2024.

- Christian Ledig, Lucas Theis, Ferenc Huszár, Jose Caballero, Andrew Cunningham, Alejandro Acosta, Andrew Aitken, Alykhan Tejani, Johannes Totz, Zehan Wang, et al. Photo-realistic single image super-resolution using a generative adversarial network. In *Proceedings of the IEEE conference on computer vision and pattern recognition*, pp. 4681–4690, 2017.
 - Jaewon Lee, Kwang Pyo Choi, and Kyong Hwan Jin. Learning local implicit fourier representation for image warping. In *European Conference on Computer Vision*, pp. 182–200. Springer, 2022.
 - Runyi Li, Xuhan Sheng, Weiqi Li, and Jian Zhang. OmniSSR: Zero-shot omnidirectional image super-resolution using stable diffusion model. In *European Conference on Computer Vision*, pp. 198–216. Springer, 2024a.
 - Weiqi Li, Shijie Zhao, Bin Chen, Xinhua Cheng, Junlin Li, Li Zhang, and Jian Zhang. ResVR: Joint rescaling and viewport rendering of omnidirectional images. In *Proceedings of the 32nd ACM International Conference on Multimedia*, pp. 78–87, 2024b.
 - Jie Liang, Hui Zeng, and Lei Zhang. Efficient and degradation-adaptive network for real-world image super-resolution. In *European Conference on Computer Vision*, pp. 574–591. Springer, 2022.
 - Jingyun Liang, Jiezhang Cao, Guolei Sun, Kai Zhang, Luc Van Gool, and Radu Timofte. SwinIR: Image restoration using swin transformer. In *Proceedings of the IEEE/CVF international conference on computer vision*, pp. 1833–1844, 2021.
 - Bee Lim, Sanghyun Son, Heewon Kim, Seungjun Nah, and Kyoung Mu Lee. Enhanced deep residual networks for single image super-resolution. In *Proceedings of the IEEE conference on computer vision and pattern recognition workshops*, pp. 136–144, 2017.
 - Xinqi Lin, Jingwen He, Ziyan Chen, Zhaoyang Lyu, Bo Dai, Fanghua Yu, Yu Qiao, Wanli Ouyang, and Chao Dong. DiffBIR: Toward blind image restoration with generative diffusion prior. In *European conference on computer vision*, pp. 430–448. Springer, 2024.
 - Cagri Ozcinar, Aakanksha Rana, and Aljosa Smolic. Super-resolution of omnidirectional images using adversarial learning. In 2019 IEEE 21st International Workshop on Multimedia Signal Processing (MMSP), pp. 1–6. IEEE, 2019.
 - Vaishnav Potlapalli, Syed Waqas Zamir, Salman H Khan, and Fahad Shahbaz Khan. PromptIR: Prompting for all-in-one image restoration. *Advances in Neural Information Processing Systems*, 36:71275–71293, 2023.
 - Xuelin Shen, Yitong Wang, Silin Zheng, Kang Xiao, Wenhan Yang, and Xu Wang. Fast omnidirectional image super-resolution: Adapting the implicit image function with pixel and semantic-wise spherical geometric priors. In *Proceedings of the AAAI Conference on Artificial Intelligence*, volume 39, pp. 6833–6841, 2025.
 - Sanghyun Son and Kyoung Mu Lee. SRWarp: Generalized image super-resolution under arbitrary transformation. In *Proceedings of the IEEE/CVF conference on computer vision and pattern recognition*, pp. 7782–7791, 2021.
 - Sanghyun Son, Jaeha Kim, Wei-Sheng Lai, Ming-Hsuan Yang, and Kyoung Mu Lee. Toward real-world super-resolution via adaptive downsampling models. *IEEE transactions on pattern analysis and machine intelligence*, 44(11):8657–8670, 2021.
 - Yule Sun, Ang Lu, and Lu Yu. Weighted-to-spherically-uniform quality evaluation for omnidirectional video. *IEEE signal processing letters*, 24(9):1408–1412, 2017.
 - Yuchuan Tian, Hanting Chen, Chao Xu, and Yunhe Wang. Image processing GNN: Breaking rigidity in super-resolution. In *Proceedings of the IEEE/CVF conference on computer vision and pattern recognition*, pp. 24108–24117, 2024.
 - Jiangang Wang, Yuning Cui, Yawen Li, Wenqi Ren, and Xiaochun Cao. Omnidirectional image super-resolution via bi-projection fusion. In *Proceedings of the AAAI Conference on Artificial Intelligence*, volume 38, pp. 5454–5462, 2024.

- Longguang Wang, Yingqian Wang, Xiaoyu Dong, Qingyu Xu, Jungang Yang, Wei An, and Yulan Guo. Unsupervised degradation representation learning for blind super-resolution. In *Proceedings of the IEEE/CVF conference on computer vision and pattern recognition*, pp. 10581–10590, 2021a.
 - Xintao Wang, Liangbin Xie, Chao Dong, and Ying Shan. Real-ESRGAN: Training real-world blind super-resolution with pure synthetic data. In *Proceedings of the IEEE/CVF international conference on computer vision*, pp. 1905–1914, 2021b.
 - Yunxuan Wei, Shuhang Gu, Yawei Li, Radu Timofte, Longcun Jin, and Hengjie Song. Unsupervised real-world image super resolution via domain-distance aware training. In *Proceedings of the IEEE/CVF conference on computer vision and pattern recognition*, pp. 13385–13394, 2021.
 - Rongyuan Wu, Tao Yang, Lingchen Sun, Zhengqiang Zhang, Shuai Li, and Lei Zhang. SeeSR: Towards semantics-aware real-world image super-resolution. In *Proceedings of the IEEE/CVF conference on computer vision and pattern recognition*, pp. 25456–25467, 2024.
 - Jianxiong Xiao, Krista A Ehinger, Aude Oliva, and Antonio Torralba. Recognizing scene viewpoint using panoramic place representation. In 2012 IEEE conference on computer vision and pattern recognition, pp. 2695–2702. IEEE, 2012.
 - Cuixin Yang, Rongkang Dong, Jun Xiao, Cong Zhang, Kin-Man Lam, Fei Zhou, and Guoping Qiu. Geometric distortion guided transformer for omnidirectional image super-resolution. *IEEE Transactions on Circuits and Systems for Video Technology*, 2025.
 - Zhixiong Yang, Jingyuan Xia, Shengxi Li, Xinghua Huang, Shuanghui Zhang, Zhen Liu, Yaowen Fu, and Yongxiang Liu. A dynamic kernel prior model for unsupervised blind image superresolution. In *Proceedings of the IEEE/CVF conference on computer vision and pattern recognition*, pp. 26046–26056, 2024.
 - Youngho Yoon, Inchul Chung, Lin Wang, and Kuk-Jin Yoon. SphereSR: 360° image superresolution with arbitrary projection via continuous spherical image representation. In *Proceedings* of the IEEE/CVF Conference on Computer Vision and Pattern Recognition, pp. 5677–5686, 2022.
 - Fanghua Yu, Xintao Wang, Mingdeng Cao, Gen Li, Ying Shan, and Chao Dong. OSRT: Omnidirectional image super-resolution with distortion-aware transformer. In *Proceedings of the IEEE/CVF Conference on Computer Vision and Pattern Recognition*, pp. 13283–13292, 2023.
 - Fanghua Yu, Jinjin Gu, Zheyuan Li, Jinfan Hu, Xiangtao Kong, Xintao Wang, Jingwen He, Yu Qiao, and Chao Dong. Scaling up to excellence: Practicing model scaling for photo-realistic image restoration in the wild. In *Proceedings of the IEEE/CVF conference on computer vision and pattern recognition*, pp. 25669–25680, 2024.
 - Kai Zhang, Jingyun Liang, Luc Van Gool, and Radu Timofte. Designing a practical degradation model for deep blind image super-resolution. In *Proceedings of the IEEE/CVF International Conference on Computer Vision*, pp. 4791–4800, 2021.
 - Yulun Zhang, Kunpeng Li, Kai Li, Lichen Wang, Bineng Zhong, and Yun Fu. Image superresolution using very deep residual channel attention networks. In *Proceedings of the European* conference on computer vision (ECCV), pp. 286–301, 2018.
 - Yufeng Zhou, Mei Yu, Hualin Ma, Hua Shao, and Gangyi Jiang. Weighted-to-spherically-uniform ssim objective quality evaluation for panoramic video. In 2018 14th IEEE International Conference on Signal Processing (ICSP), pp. 54–57. IEEE, 2018.

A APPENDIX

A.1 USE OF LLMS

We employed large language models solely for minor language polishing and code reproduction. All research ideas, experimental designs, analyses, and conclusions were independently developed by the authors.

A.2 EQUIRECTANGULAR PROJECTION

In this section, we follow the coordinate representation in the main paper and provide a rigorous derivation of the ERP and its associated distortion analysis. More precisely, spherical coordinates are defined as (ρ, θ, ϕ) , where $\theta \in (0, 2\pi)$ and $\phi \in (0, \pi)$ denote longitude and latitude, respectively. The corresponding planar horizontal and vertical coordinates are parameterized as (u, v).

A.2.1 GEOMETRIC TRANSFORMATION

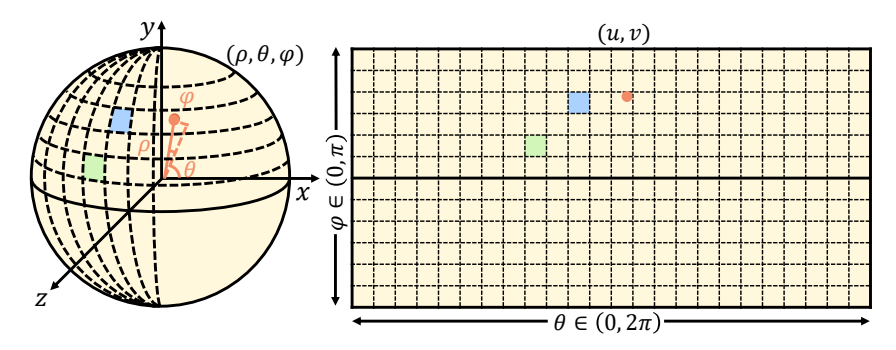


Figure 7: Geometric explanation of transforming between the ideal spherical surface and ERP plane.

The coordinate transformation between 3D sphere and 2D plane is defined as:

$$\begin{cases} \rho = \sqrt{x^2 + y^2 + z^2}, \\ \theta = \arctan(y/x), \\ \phi = \arcsin(z/\rho). \end{cases} \begin{cases} x = \rho \cos(\phi) \cos(\theta), \\ y = \rho \cos(\phi) \sin(\theta), \\ z = \rho \sin(\phi). \end{cases}$$
 (7)

$$\begin{cases} \theta = (u/W - 0.5)2\pi, \\ \phi = (0.5 - v/H)\pi. \end{cases} \begin{cases} u = (\theta/2\pi + 0.5)W, \\ v = (0.5 - \phi/\pi)H. \end{cases}$$
(8)

where (x, y, z) are world coordinates responding to spherical coordinates (ρ, θ, ϕ) , H and W indicate the height and width (in pixels) of the ERP omnidirectional image (ODI). Fig. 7 provides an illustrative example of the forward ERP projection and its exact inverse back-projection between the spherical and planar domains.

A.2.2 PROJECTION DISTORTION

Inspired by Sun et al. (2017), we quantify the projection distortion via the local stretching ratio (STR) induced by the mapping from the spherical surface to the ERP plane. As shown in Fig. 7, assuming a spherical element $d\theta d\phi$ whose area is $\delta S(\theta,\phi)$. After ERP, the planar area element dudv with a center point (u,v) is defined as $\delta P(u,v)$. The differential relation between element $d\theta d\phi$ and $\delta P(u,v)$ is captured by the Jacobian determinant $dudv = J(\theta,\phi)d\theta d\phi$ as follows:

$$J(\theta,\phi) = \frac{\partial(u,v)}{\partial(\theta,\phi)} = \begin{vmatrix} \frac{\partial(u)}{\partial(\theta)} & \frac{\partial(v)}{\partial(\phi)} \\ \frac{\partial(u)}{\partial(\theta)} & \frac{\partial(v)}{\partial(\phi)} \\ \frac{\partial(u)}{\partial(\theta)} & \frac{\partial(v)}{\partial(\phi)} \end{vmatrix}. \tag{9}$$

Dataset	SUN360 Dataset						
Method	PSNR (dB)↑/ SSIM↑	WS-PSNR (dB)↑/ WS-SSIM↑	Params. (M)↓	FLOPs (T)↓	Runtime (s)↓		
360-SS	23.02 / 0.5943	22.44 / 0.5872	0.19	0.73	0.21		
Real-ESRGAN	23.07 / 0.5922	22.51 / 0.5870	16.70	2.35	0.69		
SwinIR	23.66 / 0.6439	23.14 / 0.6414	11.67	1.70	0.75		
HAT	23.67 / 0.6444	23.15 / 0.6419	20.33	2.84	0.51		
PromptIR	23.69 / 0.6464	23.17 / 0.6438	48.85	0.67	0.47		
OSŔT	23.82 / 0.6484	23.32 / 0.6464	6.02	0.79	1.33		
BPOSR	23.75 / 0.6459	23.22 / 0.6430	2.07	0.32	0.42		
AdaIR	23.85 / 0.6502	23.35 / 0.6486	28.90	0.96	0.38		
DSOSR(Ours)	24.00 / 0.6528	$\overline{23.50}$ / $\overline{0.6513}$	3.50	<u>0.55</u>	<u>0.34</u>		

Table 4: Quantitative $\times 4$ real-world ODI-SR and computational efficiency comparison on the SUN360 dataset.

Furthermore, the area $\delta P(u,v)$ and $\delta S(\theta,\phi)$ are equal to |dudv| and $d\theta d\phi \cos(\phi)$, respectively. Therefor, the area stretching ratio $\mathrm{STR}(u,v)$ can be derived as:

$$STR(u, v) = \frac{\delta S(\theta, \phi)}{\delta P(u, v)} = \frac{|d\theta d\phi| \cos(\phi)}{|du dv|} = \frac{\cos(\phi)}{\left|\frac{\partial (u, v)}{\partial (\theta, \phi)}\right|}$$

$$= \frac{\cos(\phi)}{|J(\theta, \phi)|}.$$
(10)

From Eq. 8, we can conclude that $|J(\theta,\phi)|=1$, thus obtaining $STR(u,v)=\cos(\phi)$ for ERP. As a result, ERP distortions are fully characterized by latitudes. As latitude increases, STR decreases, and distortion becomes more severe. Therefore, we could formulate STR as latitude-related pixel weights ranging from 0 to 1:

$$W_{lat}(u,v) = \cos((v - (H/2) + 0.5)\pi/H). \tag{11}$$

A.3 QUANTITATIVE COMPARISON RESULTS

Experimental results on the SUN360 dataset and the computational efficiency are summarized in Tab. 4. Relative to other methods with a large number of parameters, DSOSR achieves a faster running speed while preserving the best SR quality, striking an effective complexity-performance trade-off.